Accepted Manuscript

Thermoelastic fracture modelling in 2D by an adaptive cracking particle method without enrichment functions

Weilong Ai, Charles E. Augarde

PII: S0020-7403(19)30228-0
DOI: https://doi.org/10.1016/j.ijmecsci.2019.06.033
Reference: MS 4987

To appear in: *International Journal of Mechanical Sciences*

Received date: 18 January 2019
Revised date: 20 May 2019
Accepted date: 19 June 2019

Please cite this article as: Weilong Ai, Charles E. Augarde, Thermoelastic fracture modelling in 2D by an adaptive cracking particle method without enrichment functions, *International Journal of Mechanical Sciences* (2019), doi: https://doi.org/10.1016/j.ijmecsci.2019.06.033

Highlights

- An adaptive cracking particle method has been developed for thermoelastic fracture problems.
- Crack discontinuities are handled by the visibility criterion rather than enrichment functions, which can avoid extra unknowns and ill-conditioned system stiffness matrix.
- Thermal gradients around crack tips are captured by dense groups of particles, which are generated by an h-adaptivity approach.
- Abilities to model multiple crack propagation under both mechanical and thermal loadings.

Thermoelastic fracture modelling in 2D by an adaptive cracking particle method without enrichment functions

Weilong Ai[a,b,*], Charles E. Augarde[a]

[a] *Department of Engineering, Durham University, South Road, Durham, DH1 3LE, UK*
[b] *Dyson School of Design Engineering, Imperial College London, SW7 2DB, UK*

Abstract

Thermoelastic fracture of brittle materials is a key concern for many types of engineering structures such as aerospace components and pressure vessels. These problems present difficulties in modelling as they involve coupling of the effects of thermal and mechanical loadings, and usually material behaviours are strongly discontinuous at crack locations, and highly nonlinear during crack propagation. Most current numerical methods applied to these problems use enrichment functions to model discontinuities of temperature and stresses at cracks, however, these enrichments bring extra unknowns into the model and can lead to numerical difficulties in attempting solutions. In this paper, an adaptive cracking particle method is developed for thermoelastic fracture. The method is meshless, so crack discontinuities can be introduced by modifying the influence domains of particles, rather than through external enrichments. Another benefit is an easy implementation of h-adaptivity, since no transition is required for different densities of particles, and it is easy to build dense groups of particles around crack tips. The results demonstrate that this new method can provide the same level of accuracy as others that employ enrichment functions, but using fewer degrees of freedom. A number of examples show the flexibility of the new method to model a range of thermoelastic problems in 2D including multiple cracks and crack propagation.

Keywords: thermal-mechanical coupling, adaptivity, cracking particle method, meshless, crack propagation

*Corresponding author
Email address: weilong.ai@outlook.com (Weilong Ai)

1. Introduction

The study of thermoelastic fracture mechanics is of great importance in the design of structures under coupled mechanical and thermal loadings, including aerospace components, turbines and nuclear vessels. When heat travels across a crack, thermal gradients are set up in the neighbourhood of the crack tip, as well as thermal stresses [1]. The thermal stress concentration generated around the crack tip can lead to crack propagation and sudden failure without a change in the mechanical loading. For a crack in a thermoelastic solid, Sih (1962) [1] found that the local character of thermal stresses at the crack tip is of the same nature as the field from mechanical loading, and therefore Williams' expansions [2] for the asymptotic crack tip displacement field are applicable for thermally-induced stresses. In simplified studies of steady heat flux, crack surfaces can be considered to be either fully insulated or perfectively conductive [3, 4]. This is clearly an additional concern in thermoelastic problems, which is distinct from purely mechanical situations. More complex models exist, e.g. a partial insulation crack model has been developed in [5, 6], where the cracked zone is considered to contain a medium capable of conducting heat, e.g. air inside the crack opening domain acting as a thermal conduction medium. The partial insulation coefficient developed in these papers has a nonlinear relationship to the applied mechanical loading and to heat flux [6]. In recent decades, cracking under steady thermal loading has been studied using conventional numerical methods, and much of the development is similar to the development of non-thermal computational fracture. Examples of early numerical analysis of thermoelastic fracture mechanics use the finite element method (FEM) as in [7, 8], where discontinuities of both temperature and displacement at cracks are modelled by element interfaces, so the issue of remeshing during crack propagation remains [9]. The boundary element method (BEM) is an alternative (as in [10]), but meets dilemmas for modelling thermal nonlinearity [11]. Much success has been achieved via the use of enrichment functions within finite elements and meshless methods to model thermal fracture following their success for the purely mechanical case, for instance, in the extended finite element method (XFEM) [4, 12, 13], the element free Galerkin method (EFGM) [14–17], the numerical manifold method (NMM) [18, 19], and the isogeometric analysis method (IGA) [20]. These methods have been used to solve thermoelastic fracture problems including dynamic cracks [13], ductile cracks [21], interface cracks at bimaterial bodies [14] and fatigue fracture in railway brake discs [22]. The

scaled boundary finite element method (SBFEM) has been used for thermal fracture with a series of power functions to handle the stress concentrations at a crack tip [23, 24], however remeshing cannot be avoided for modelling crack propagation [25, 26]. In the XFEM, the benefits of using high order crack tip enrichments to improve accuracy for thermoelastic problems have been shown to be greater than for purely mechanical elastic problems, as mentioned in Zamani et al. (2010) [12]. However, the use of these enrichment functions brings extra unknowns to the problem, as both thermal and mechanical fields require a set of enrichment terms to model crack discontinuities in temperature and displacement respectively. This increase in the number of unknowns and can lead to numerical difficulties such as ill-conditioned linear systems requiring solutions [27], where possible solutions are obtained either using quasi-orthogonalization of enrichment functions [28, 29] or decomposing the system stiffness matrix to remove the diagonal zeros [30]. Alternatively, meshless methods can model crack discontinuities by disabling the influence between nodes on the two sides of the crack, which can avoid the use of enrichment functions, an advantage over element-based methods. No extra unknowns are introduced into the model, therefore meshless methods are suitable for crack problems under separate or combined thermal and mechanical loadings. Barbieri [31, 32] developed approaches with enriched weight functions to handle crack discontinuities in meshless methods, however tracking the geometry of cracks is required to build the enrichment functions, e.g. calculating the distance to crack tips, which is computationally expensive for multiple cracks and 3D crack problems.

In this paper, a novel weak form-based meshless method developed by the authors [33] is extended to thermoelastic problems in 2D. This method models cracks using "cracking particles" which are meshless nodes with certain properties. The discontinuity created by the presence of a crack is modelled using a simple visibility criterion which also handles temperature discontinuities at cracks, and no enrichment functions are needed. Accurate modelling of sharp thermal stress gradients around crack tips is achieved by an h-adaptivity approach, which generates dense groups of particles around crack tips and provides good control of the overall number of degrees of freedom. The paper is organised as follows. A brief review of current methods using enrichment functions for thermal discontinuities is included in Section 2. Then, an alternative to these enrichments is presented in Section 3 using the cracking particle method (CPM), where the h-adaptivity approach for a

temperature field is introduced. The method is applied to several problems to demonstrate its abilities and is shown to be suitable for modelling multiple crack propagation under thermal loadings.

2. Review of enriched numerical approaches for cracks under thermal loadings

External enrichment functions have been widely used in numerical methods including the XFEM [4, 12, 13] and the EFGM [14–17] to model the temperature discontinuities at cracks. Generally, two different types of cracks are studied in steady heat flux problems namely adiabatic and isothermal cracks, and the two cases result in different enrichment functions, which are applied according to the boundary conditions of the problem. The former assumes that both temperature and displacement fields are ideally discontinuous at the crack surface, while in the latter case, crack surfaces are perfectly thermally conductive and are maintained at a specific temperature, although the cracks still block the heat flux, and displacement is still discontinuous across the cracks. Partially insulated cracks are in between these two cases but are not covered in this paper.

2.1. Adiabatic cracks

In an adiabatic crack, a node located to one side of the crack has no influence on the other side in the temperature approximation. The heat flux is singular at the crack tip with the singularity $1/\sqrt{r}$ as in [1], where r is the distance to the crack tip, and is similar to the stress singularity at the crack tip for mechanical loading. The leading terms of the asymptotic expansion for temperature T and heat flux $\mathbf{q}$ near to an adiabatic crack tip are given in Yosibash (1996) [34] as

$$T = -\frac{K_T}{k_T}\sqrt{\frac{2r}{\pi}}\sin\frac{\theta}{2}, \qquad \mathbf{q} = \frac{K_T}{\sqrt{2\pi r}}[\sin\frac{\theta}{2}, \cos\frac{\theta}{2}]^{\mathrm{T}}, \tag{1}$$

where K_T is the thermal stress intensity factor, k_T is the thermal conductivity, and r and θ are local polar coordinates centred at the crack tip. Due to the local character of temperature in Equation (1), the temperature approximation is

$$T^h(\mathbf{x}) = \sum_{i=1}^{n}\Phi_i(\mathbf{x})T_i + \sum_{i=1}^{n_1}\Phi_i(\mathbf{x})H(\mathbf{x})b_i + \sum_{i=1}^{n_c}\Phi_i(\mathbf{x})\sqrt{r}\sin(\frac{\theta}{2})a_i, \tag{2}$$

where $\Phi_i(\mathbf{x})$ is a shape function, $T^h(\mathbf{x})$ is the temperature approximation, $\mathbf{x}$ is a vector of coordinates i.e. $\mathbf{x} = [x, y]$ in 2D, T_i is the temperature of the ith particle, $H(\mathbf{x})$ is the sign function, a_i and b_i are extra

unknowns, and n, n_1 and n_c are the numbers of nodes with influence domains covering $\mathbf{x}$, cut by the crack and including the crack tip respectively.

2.2. Isothermal cracks

The isothermal case differs from the adiabatic case in the angular variation of the temperature field. The leading terms of the asymptotic expansion near to an isothermal crack tip [4] become

$$T = -\frac{K_T}{k_T}\sqrt{\frac{2r}{\pi}}\cos\frac{\theta}{2}, \qquad \mathbf{q} = \frac{K_T}{\sqrt{2\pi r}}[\cos\frac{\theta}{2}, \sin\frac{\theta}{2}]^{\mathrm{T}}. \tag{3}$$

Analogically, the temperature approximation becomes

$$T^h(\mathbf{x}) = \sum_{i=1}^{n}\Phi_i(\mathbf{x})T_i + \sum_{i=1}^{n_1}\Phi_i(\mathbf{x})H(\mathbf{x})b_i + \sum_{i=1}^{n_c}\Phi_i(\mathbf{x})\sqrt{r}\cos(\frac{\theta}{2})a_i. \tag{4}$$

The sign function $H(\mathbf{x})$ in the XFEM is not applicable for an isothermal crack, since the temperature on the crack surface is continuous (but not the heat flux). $H(\mathbf{x})$ should be continuous across the crack surface with a discontinuous derivative, have a maximum value along the crack surface and become zero away from the crack. These properties can be delivered using the normal level set function to replace $H(\mathbf{x})$ as described in Duflot (2008) [4] as

$$H'(\mathbf{x}) = \sum_{\mathrm{i}=1}^{n_1}\Phi_i(\mathbf{x})|\phi_i| - |\phi(\mathbf{x})|, \tag{5}$$

where $\phi(\mathbf{x})$ is the level set function describing the distance to the crack surface.

To summarise, in simple problems involving temperature fields interacting with existing cracks, two types of cracks have been developed by assuming the crack to be thermally conductive or not, which leads to different types of temperature distributions. This brings challenges to numerical methods using external enrichment functions, which should be modified accordingly to capture the discontinuities caused by cracks. As indicated above and demonstrated in Equations (2) and (4), extra unknowns are required by these enrichment functions for both thermal and mechanical fields. However, an alternative meshless approach can be taken that entirely avoids the use of enrichment functions as described in the following section.

3. A cracking particle method requiring no enrichment functions

While finite element methods such as the XFEM have received much attention for modelling fracture problems, meshless methods using only nodes (or particles) in problem discretisation have also been prominent since they remove the need for element connectivity to be generated, and have major advantages when it comes to adaptivity. In meshless methods, connectivity between nodes is achieved by defining overlapping domains adjacent to the nodes over which they have influence, i.e. domains of influence or support. The most well-known weak form-based meshless method is the EFGM from which the cracking particle method was developed. The CPM models a crack path using directional segments that are centred at nodes, as shown in Figure 1 (a-b). It is a highly flexible approach able to model multiple cracks and branching. Discontinuities at cracks are simulated by using the so-called visibility criterion. This applies a "line-of-sight" check to alter the influence domain of a node if it overlaps with a crack as presented in Figure 1 (c) and so removes the need for any enrichment to do this job. The issue of having to deal with problems in which there are strong stress singularities at crack tips, which is dealt with in enriched approaches by altering the basis functions, is dealt with here by an h-adaptivity approach allowing a very fine discretisation around a crack tip. This will be shown to work satisfactorily later in the paper. The CPM was originally presented by Rabczuk and Belytschko (2004) [35] and has since been applied to model 3D cracks [36–38], dynamic fracture [39], ductile fracture [40], shear bands [41, 42] and multiple cracks [43]. Here the CPM is applied to thermoelastic fracture problems, where only the adiabatic crack is studied since there is little difference in the visibility criterion process for checking connectivities of particles between the adiabatic and isothermal situations. An isothermal crack differs in that its surface is maintained at a specified temperature, which can be handled with methods for essential boundary conditions such as Lagrange multipliers [14], widely used in meshless methods to impose essential boundary conditions [44].

3.1. Displacement and temperature approximation

In the CPM, the displacement field is approximated by the moving least squares (MLS) approach [44] using a set of sampling points (and their locations). In the same fashion, the temperature field can be approximated

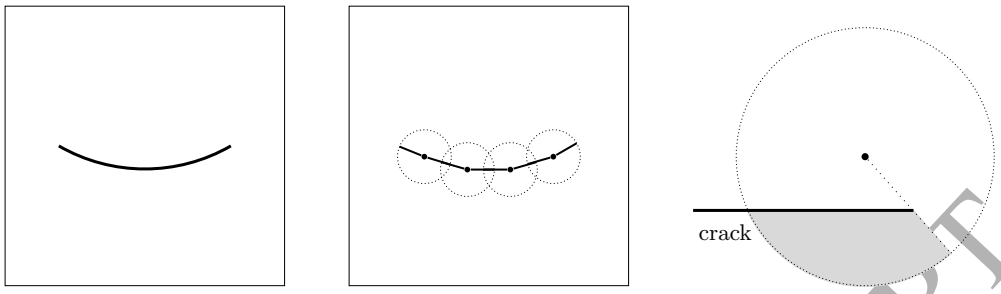

(a) curved crack (b) cracking particles (c) visibility criterion

Figure 1: Crack description by the cracking particle method.

with the same MLS approach in [14, 16] as

$$u^h(\mathbf{x}) = \sum_{i=1}^{n} \Phi_i(\mathbf{x}) u_i, \qquad T^h(\mathbf{x}) = \sum_{i=1}^{n} \Phi_i(\mathbf{x}) T_i, \tag{6}$$

where $u^h(\mathbf{x})$ and $T^h(\mathbf{x})$ are approximations of displacement and temperature respectively, u_i is the nodal value of displacement at the ith particle which can be the displacement along x or y axis, T_i is the nodal value for temperature and $\Phi_i(\mathbf{x})$ is the shape function obtained by the MLS approximation.

3.2. Weak form for mechanical and thermal governing equations

The CPM uses the EFGM to discretise the problem domain, and the latter for elastic problems is well known, so the details will not be repeated here but can be found in [33, 44]. The following includes the discretised governing equations for the CPM, to demonstrate the similarities between the modelling of the mechanical and the thermal fields. It is notable that the shape functions of the EFGM cannot meet the Kronecker delta property, and essential boundary conditions cannot be imposed directly, but through methods such as the Lagrange multiplier approach [44]. The weak form of the equilibrium equation for the mechanical field is

$$\int_{\Omega} \delta\boldsymbol{\varepsilon}^{\mathrm{T}} \cdot \boldsymbol{\sigma} \, \mathrm{d}\Omega - \int_{\Gamma_u} \delta\boldsymbol{\lambda}^{\mathrm{T}} \cdot (\mathbf{u} - \bar{\mathbf{u}}) \, \mathrm{d}\Gamma_u - \int_{\Gamma_u} \delta\mathbf{u}^{\mathrm{T}} \cdot \boldsymbol{\lambda} \, \mathrm{d}\Gamma_u = \int_{\Omega} \delta\mathbf{u}^{\mathrm{T}} \cdot \mathbf{b} \, \mathrm{d}\Omega + \int_{\Gamma_t} \delta\mathbf{u}^{\mathrm{T}} \cdot \bar{\mathbf{t}} \, \mathrm{d}\Gamma_t, \tag{7}$$

and the discretised governing equation is

$$\begin{bmatrix} \mathbf{K} & \mathbf{G} \\ \mathbf{G}^{\mathrm{T}} & \mathbf{0} \end{bmatrix} \begin{Bmatrix} \mathbf{u} \\ \boldsymbol{\lambda} \end{Bmatrix} = \begin{Bmatrix} \mathbf{f} \\ \mathbf{R} \end{Bmatrix}, \tag{8}$$

where $\mathbf{u}$ and $\boldsymbol{\lambda}$ are vectors of displacement and Lagrange multipliers respectively, $\boldsymbol{\sigma}$ and $\boldsymbol{\varepsilon}$ are vectors of Cauchy stress and strain respectively using Voigt notation, $\bar{\mathbf{u}}$ is a vector of displacement constraints, $\mathbf{b}$ is a vector of body forces and $\bar{\mathbf{t}}$ is a vector of external forces. $\mathbf{K}$ and $\mathbf{G}$ are stiffness matrices for displacement and Lagrange multipliers respectively, $\mathbf{f}$ is a vector of force acting at each degree of freedom, and $\mathbf{R}$ is a vector of constraint at displacement boundaries. $\mathbf{K}$, $\mathbf{G}$, $\mathbf{f}$ and $\mathbf{R}$ are calculated in [33] as

$$\mathbf{K}_{ij} = \int_{\Omega} \mathbf{B}_i^{\mathrm{T}} \mathbf{D} \mathbf{B}_j \mathrm{d}\Omega, \qquad \mathbf{G}_{ik} = -\int_{\Gamma_u} \Phi_i N_k \mathrm{d}\Gamma_u, \tag{9a}$$

$$\mathbf{f}_i = \int_{\Gamma_t} \Phi_i \bar{\mathbf{t}} \, \mathrm{d}\Gamma_t + \int_{\Omega} \Phi_i \mathbf{b} \mathrm{d}\Omega + \int_{\Omega} \mathbf{B}_i^{\mathrm{T}} \mathbf{D} \boldsymbol{\varepsilon}_T \mathrm{d}\Omega, \qquad \mathbf{R}_k = -\int_{\Gamma_u} N_k \bar{\mathbf{u}} \mathrm{d}\Gamma_u, \tag{9b}$$

where

$$\mathbf{B}_i = \begin{bmatrix} \Phi_{i,x} & 0 \\ 0 & \Phi_{i,y} \\ \Phi_{i,y} & \Phi_{i,x} \end{bmatrix}, \qquad \mathbf{D} = \frac{\bar{E}}{1-\bar{\nu}} \begin{bmatrix} 1 & \bar{\nu} & 0 \\ \bar{\nu} & 1 & 0 \\ 0 & 0 & \frac{1-\bar{\nu}}{2} \end{bmatrix}, \tag{9c}$$

$$\bar{E} = \begin{cases} E & \text{plane stress,} \\ \frac{E}{1-\nu^2} & \text{plane strain,} \end{cases} \qquad \bar{\nu} = \begin{cases} \nu & \text{plane stress,} \\ \frac{\nu}{1-\nu} & \text{plane strain.} \end{cases} \tag{9d}$$

N_k is the shape function for Lagrange multipliers constructed by Lagrangian interpolation. In Equation (9a) the subscripts i, j do not stand for the components of the matrix but for particles i and j, similar rule for i, k. The coupling between the mechanical and thermal fields is through the assumption that a material is deformed by the temperature change due to thermal expansion, e.g. the thermal strain $\boldsymbol{\varepsilon}_T$ in 2D using Voigt notation is

$$\boldsymbol{\varepsilon}_T = \alpha_T (T - T_0)[1, 1, 0]^{\mathrm{T}}, \tag{10}$$

where T_0 is the reference temperature before thermal loading and α_T is the coefficient of thermal expansion. The constitutive model in the mechanical field is therefore modified to include thermal effects, as

$$\boldsymbol{\sigma} = \mathbf{D}(\boldsymbol{\varepsilon} - \boldsymbol{\varepsilon}_T). \tag{11}$$

The force vector in the governing equation in Equation (9b) is different from the purely mechanical situations, to take the thermal effects into account.

Similarly to the mechanical field, the weak form for the conservation of thermal flows from [14] is

$$\int_{\Omega} \delta \mathbf{q}^{\mathrm{T}} \cdot \mathbf{q} \, \mathrm{d}\Omega - \int_{\Gamma_T} \delta\lambda (T - \bar{T}) \, \mathrm{d}\Gamma_T - \int_{\Gamma_T} \delta T \lambda \, \mathrm{d}\Gamma_T = \int_{\Omega} \delta T \, \bar{q} \, \mathrm{d}\Omega + \int_{\Gamma_q} \delta T \, Q \, \mathrm{d}\Gamma_q, \tag{12}$$

where $\bar{q}$ is the constraint of thermal flux with $\mathbf{q} \cdot \mathbf{n} = \bar{q}$ and Q is the heat source. The discretised equation is

$$\begin{bmatrix} \hat{\mathbf{K}} & \hat{\mathbf{G}} \\ \hat{\mathbf{G}}^{\mathrm{T}} & \mathbf{0} \end{bmatrix} \begin{Bmatrix} \mathbf{T} \\ \hat{\boldsymbol{\lambda}} \end{Bmatrix} = \begin{Bmatrix} \hat{\mathbf{f}} \\ \hat{\mathbf{R}} \end{Bmatrix}, \tag{13}$$

where the hat is used for terms in the thermal field, distinct from the corresponding terms in the mechanical governing equations. The "stiffness" matrix $\hat{\mathbf{K}}$ for the temperature, the external load $\hat{\mathbf{f}}$, $\hat{\mathbf{G}}$ and $\hat{\mathbf{R}}$ are calculated respectively in [14] as

$$\hat{\mathbf{K}}_{ij} = \int_{\Omega} \begin{bmatrix} \Phi_{i,x} \\ \Phi_{i,y} \end{bmatrix}^{\mathrm{T}} \begin{bmatrix} k_T & 0 \\ 0 & k_T \end{bmatrix} \begin{bmatrix} \Phi_{i,x} \\ \Phi_{i,y} \end{bmatrix} \mathrm{d}\Omega, \qquad \hat{\mathbf{f}}_i = \int_{\Gamma_q} \Phi_i \bar{q} \mathrm{d}\Gamma_q + \int_{\Omega} \Phi_i Q \mathrm{d}\Omega, \tag{14a}$$

$$\hat{\mathbf{G}}_{ik} = -\int_{\Gamma_u} \Phi_i N_k \mathrm{d}\Gamma_T, \qquad \hat{\mathbf{R}}_k = -\int_{\Gamma_u} N_k \bar{T} \mathrm{d}\Gamma_T, \tag{14b}$$

where k_T is the thermal conductivity.

Here mechanical and thermal governing equations are considered to be uncoupled as in [14, 45] with an implicit assumption of an infinite propagation speed of the heat wave. The temperature and displacement fields are approximated using the same set of particles for the problem discretisation. Comparing Equations (9a) and (14a), the stiffness matrices for temperature and displacement can be assembled in one loop, and shape functions and their derivatives are calculated once at each Gauss point (in the background integration cells used in the EFGM), so the computational expense of including the temperature field is not high. The whole process is demonstrated in Algorithm 1.

3.3. Adaptivity

Although crack-tip enrichments have been used in the XFEM [4, 12] and the EFGM [16, 17] to approximate the high stress gradients generated around the crack tip, there are still problems in the integration of the system stiffness, where a large number of integration points (or elements) are required in the local zone of the crack tip. The adaptivity approach is suitable for crack problems, because it can provide an optimised distribution of

Algorithm 1 Solve the temperature and displacement field

1: **for** i=1:n_g % Loop over each Gauss point **do**
2: Find all particles with support covering to the Gauss point i
3: Calculate shape functions through the MLS approximation
4: Assemble global stiffness matrix for the displacement field using Equation (9a)
5: Assemble global stiffness matrix for the temperature field using Equation (14a)
6: **end for**
7: Solve the temperature field using Equation (13)
8: Use the solution of temperatures as input, obtain the displacement field using Equation (8)

particles so both accuracy around the crack tip and calculation efficiency can be maintained. Many adaptivity approaches have been developed in the last two decades and reviews can be found in [33, 46]. The *a posteriori* h-adaptivity approach, developed by the authors specifically for the CPM [33], is here extended to thermal situations as below. Of note is the fact that the approach both refines and coarsens the discretisation, leading to high computational efficiency.

The adaptivity approach uses a *recovery*-based error estimator

$$\|E_g\| = \left\{ \frac{1}{2} \int_\Omega (\boldsymbol{\sigma}^p - \boldsymbol{\sigma}^h)^{\mathrm{T}} \mathbf{D}^{-1} (\boldsymbol{\sigma}^p - \boldsymbol{\sigma}^h) \mathrm{d}\Omega \right\}^{\frac{1}{2}}, \tag{15}$$

where $\boldsymbol{\sigma}^h$ and $\boldsymbol{\sigma}^p$ are calculated stress and "projected" stress respectively, written in Voigt notation. $\boldsymbol{\sigma}^p$ is an approximation of the exact stress in [47], as

$$\boldsymbol{\sigma}^p = \sum_{k=1}^{m} \Psi_k(\mathbf{x}) \boldsymbol{\sigma}^h(\mathbf{x}_k), \tag{16}$$

where $\Psi_k(\mathbf{x})$ are shape functions calculated by the MLS approximation using smaller supports than those for calculating $\Phi_i(\mathbf{x})$, and m is the number of particles with the smaller supports covering $\mathbf{x}$. $\Psi_k(\mathbf{x})$ are discontinuous at the cracks which are handled by the visibility criterion mentioned above. To consider the thermal effects on the problem error approximation, $\boldsymbol{\sigma}^h$ and $\boldsymbol{\sigma}^p$ in the CPM for thermoelastic problems are modified using Equation (11) to

$$\boldsymbol{\sigma}^h = \mathbf{D} \sum_{i=1}^{n} \left(\mathbf{B}_i \mathbf{u}_i - \Phi_i \alpha_T (T_i - T_0) [1,1,0]^{\mathrm{T}} \right), \tag{17a}$$

$$\boldsymbol{\sigma}^p = \sum_{k=1}^{m} \left\{ \Psi_k \mathbf{D} \sum_{i=1}^{n} \left(\mathbf{B}_i \mathbf{u}_i - \Phi_i \alpha_T (T_i - T_0)[1,1,0]^{\mathrm{T}} \right) \right\}. \tag{17b}$$

The approach for refining and coarsening particles in [33] is also applicable to thermal situations, and here a brief summary is included. The relative global error η_g is evaluated using

$$\eta_g = \frac{\|E_g\|}{\|U\|}, \quad \text{with } \|U\| = \left\{ \frac{1}{2} \int_\Omega (\boldsymbol{\sigma}^h)^{\mathrm{T}} \mathbf{D}^{-1} \boldsymbol{\sigma}^h \mathrm{d}\Omega \right\}^{1/2}. \tag{18}$$

When the global error η_g is larger than the target error η_t, the adaptive approach is enabled. The local error $\|E_i\|$ of a background cell Ω_i is estimated using Equation (15) with Ω_i replacing Ω. The relative local error is

$$\eta_i = \frac{\|E_i\|}{\|U\| / \sqrt{n_{\mathrm{cell}}}}, \tag{19}$$

where n_{cell} is the number of all background cells. Two thresholds have been used in [33] to refine or coarsen particles, as

$$\begin{cases} \eta_i > 3\eta_{\mathrm{t}} & \text{to be refined,} \\ \eta_i < \frac{1}{3}\eta_{\mathrm{t}} & \text{to be coarsened.} \end{cases} \tag{20}$$

When a cell i has $\eta_i > 3\eta_{\mathrm{t}}$, it is divided into four smaller cells and five particles are added; when four cells have $\eta_i < \frac{1}{3}\eta_{\mathrm{t}}$, they are combined to a larger cell and five particles are deleted, so the density of particles is reduced in areas where they are not needed, leading to computational efficiencies.

3.4. Interaction integration for cracks under thermal loadings

The thermal stress intensity factors are calculated by the interaction integral [48]. Compared to the interaction integration in mechanical situations [48], the difference for thermal situations is the inclusion of thermal terms as in [12, 14, 48]. The interaction integral is the superposition of two states for the J-integral: the real state (as state 1) which contains σ_{ij}, ε_{ij}, u_i, T_i; and the auxiliary state (as state 2) which excludes T_i, while the other terms are predefined as in [48]. The interaction integral is defined as

$$I^{(1,2)} = \int_A \left((\sigma_{ij}^{(1)} u_{j,1}^{(2)} + \sigma_{ij}^{(2)} u_{j,1}^{(1)} - W^{(1,2)} \delta_{1i}) q_{,i} + q \bar{\alpha}_T \sigma_{kk}^{(2)} T_{,1}^{(1)} \right) \mathrm{d}A, \quad i,j,k \in \{1,2\}, \tag{21}$$

where index notation is used with the Einstein summation. The superscripts (1) and (2) represent the terms from state 1 and state 2 respectively, $W^{(1,2)}$ is the interaction strain energy density between the two states, as

$$W^{(1,2)} = \sigma_{ij}^{(1)} \varepsilon_{ij}^{(2)} = \sigma_{ij}^{(2)} \varepsilon_{ij}^{(1)}. \tag{22}$$

Considering the relationship between the SIFs and the interaction integral, the SIFs for a mixed-mode crack are obtained by applying the specific auxiliary state, as in [12].

4. Numerical examples

Several numerical examples are presented in this section to demonstrate the performance of the proposed method. The first is an inclined crack under thermal loading, where mixed-mode fracture is considered. The second example contains a curved crack to test the abilities of the proposed method for cracks with complex geometries. Crack propagation is included in the third example, where the behaviours of a crack in a cruciform shaped plate under mechanical and thermal loadings are compared. The next example is extended from the third with one more crack, and is used to explore the performance of the proposed method for multiple cracks. A penny-shaped crack problem under thermal loading is included to demonstrate the ability of the proposed method for 3D crack problems. Unless stated otherwise, all examples are under plane strain assumptions with linear elastic material properties: Young's modulus $E = 200$ GPa, Poisson's ratio $\nu = 0.3$, thermal conductivity $k_T = 100$ W/(m°C) and coefficient of thermal expansion $\alpha_T = 10^{-5}$ °C^{-1}, combinations of which are used to normalise the results, and the reference environment temperature is zero. For all examples, a circular influence domain is used for every particle, and the ratio of the radius to the average particle distance is $d_s = 2.2$. A 4th order spline function is used as the weight function in the MLS approximation (where a discussion of different support sizes and weight functions can be found in [49]). Rigid body translation and rotation are fixed as in [50] by setting

$$\int_\Omega u_x \mathrm{d}\Omega = 0, \quad \int_\Omega u_y \mathrm{d}\Omega = 0, \quad \int_\Omega \frac{\partial u_x}{\partial y} - \frac{\partial u_y}{\partial x} \mathrm{d}\Omega = 0, \tag{23}$$

where u_x and u_y are horizontal and vertical displacements respectively. These boundary conditions are imposed on the weak form by Lagrange multipliers with only three extra unknowns.

4.1. Inclined central crack

An inclined central crack is considered in a rectangular plate as shown in Figure 2. The configuration of this problem is $w = 0.1$ m, $h = 0.5w$, $a = 0.3w$. The top of the plate is at a high temperature $\bar{T} = 100$ °C, while

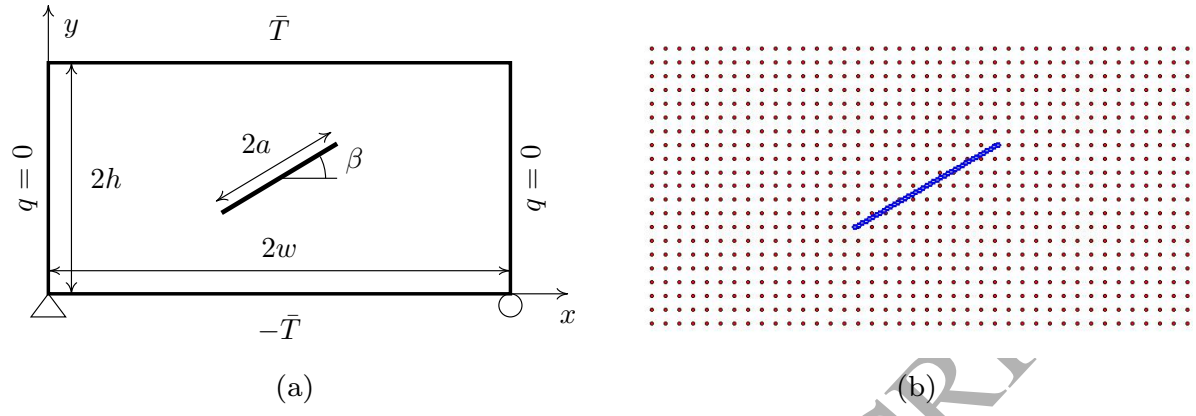

Figure 2: An inclined central crack under thermal loading: (a) configuration; (b) initial particle arrangement, with blue points for cracking particles.

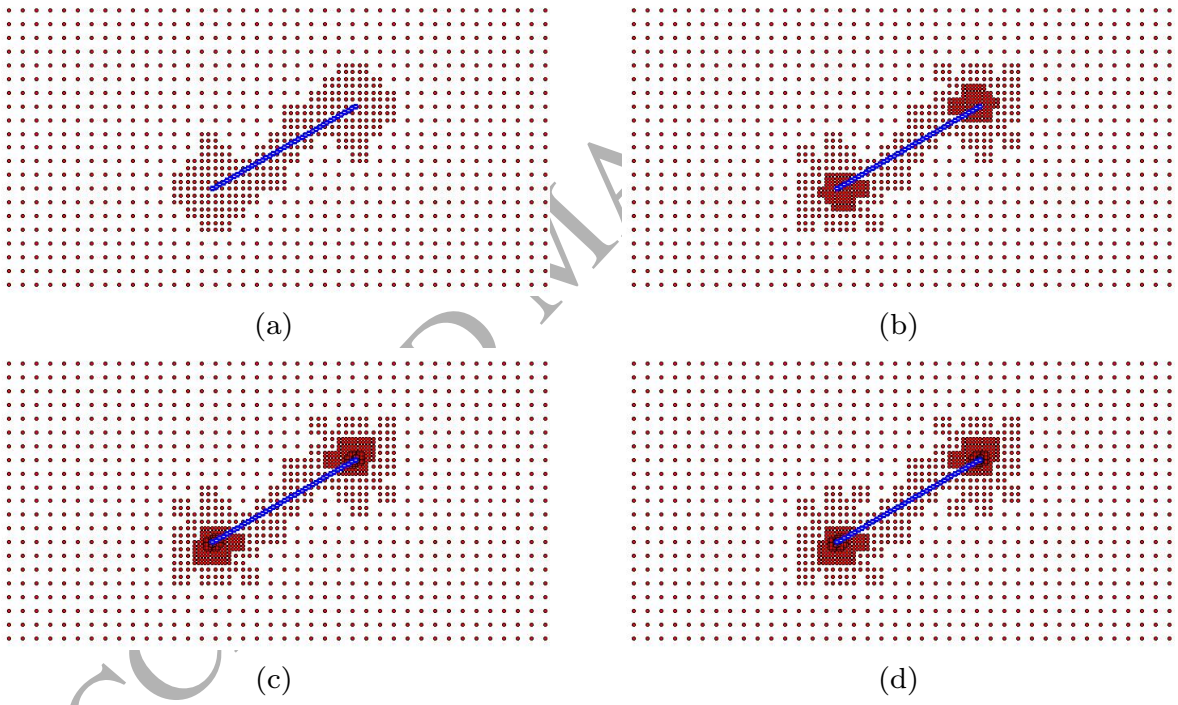

Figure 3: Adaptive particle arrangements for the inclined central crack (in blue, $\beta = 30°$) under thermal loading: (a) step 1; (b) step 2; (c) step 4; (d) step 7.

the bottom is at a low temperature $-\bar{T}$. The heat flux on the two sides of the plate is zero. The problem is initially discretised by 21×41 particles with 41 particles (shown in blue) along the crack as in Figure 2 (b).

The target error for the adaptivity approach is $\eta_t = 0.06$, and adaptive particle arrangements are given in Figure 3, where particle refinement is executed automatically around the two crack tips. Figures 4 (a-c)

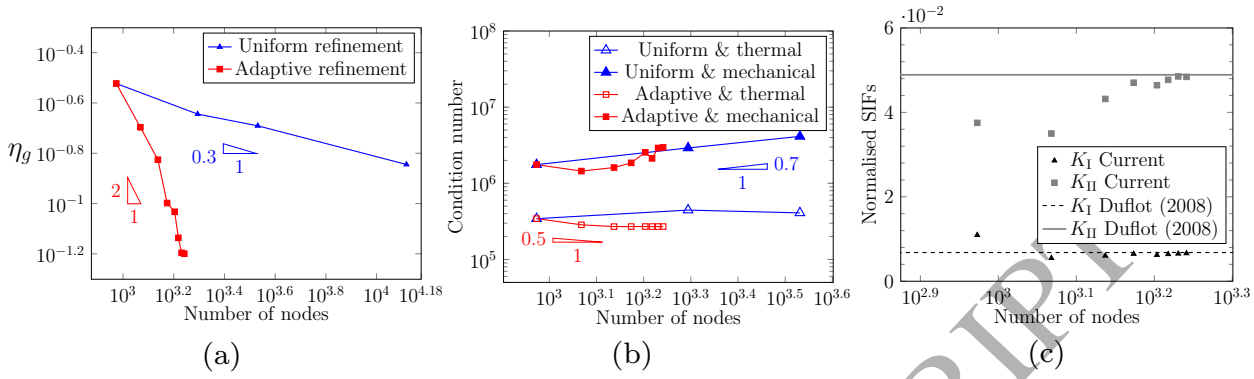

Figure 4: Adaptive results for the inclined central crack under thermal loading: (a) convergence rate for error; (b) condition number and (c) SIFs.

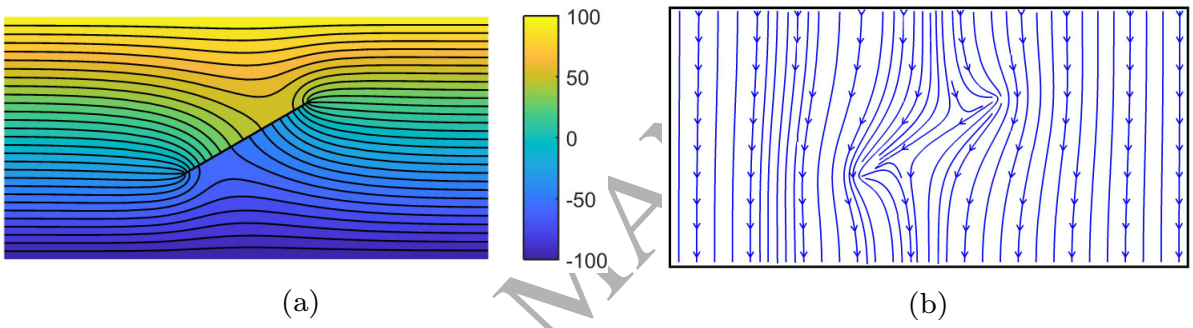

Figure 5: Thermal results of the inclined central crack: (a) temperature profile (°C); (b) heat flux.

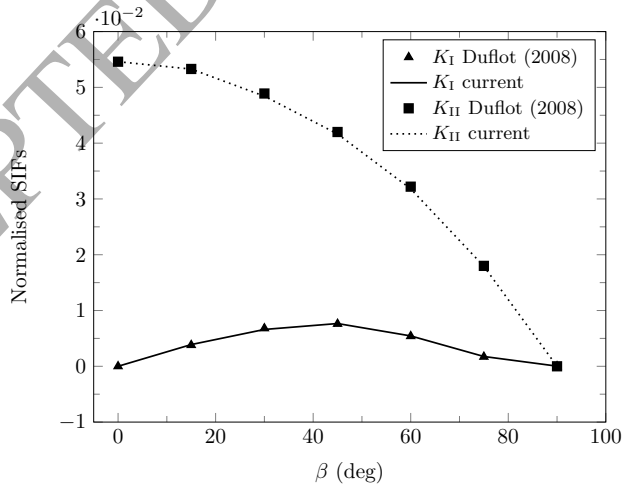

Figure 6: Normalised stress intensity factors for various crack inclinations.

illustrate the results during the adaptive steps, where it is shown that the convergence rate of error for the adaptivity approach is much higher than that for uniform refinement, and results for the SIFs converge to the

Table 1: Validation of calculated SIFs for the inclined crack under thermal loading

	CPM		HXFEM [12]		XFEM [4]		BEM [10]	
θ	K'_{I}	K'_{II}	K'_{I}	K'_{II}	K'_{I}	K'_{II}	K'_{I}	K'_{II}
0°	0.00000	0.05532	0.00000	0.05471	0.00000	0.05460	0.00000	0.05400
30°	0.00664	0.04894	0.00670	0.04873	0.00680	0.04890	0.00640	0.04800
60°	0.00561	0.03200	0.00544	0.03209	0.00540	0.03220	0.00490	0.03200

reference values during adaptive steps. Figures 4 (b) presents the second norm condition number of the thermal and mechanical system "stiffness" matrix in Equations (13) and (8) respectively, where adaptive refinement results in smaller condition numbers than uniform refinement. The SIFs at one crack tip are normalised by

$$K'_n = \frac{K_n}{\alpha_T \bar{T} E} \cdot \frac{h}{w\sqrt{2w}}, \quad n \in \{\mathrm{I}, \mathrm{II}\}. \tag{24}$$

and in Table 1 are compared with the results from other methods, including the XFEM from Duflot [4], the XFEM with high order enrichment functions (marked as HXFEM) from Zamani et al. [12] and the BEM from Prasad et al. [10]. The proposed method gives results with the same level of accuracy as using enrichment functions, and with adaptivity the maximum number of particles here is 1744 versus 1891 rectangular elements in the HXFEM [12], and 7000 triangular elements in the XFEM [4]. Figures 5 (a-b) illustrate the temperature distribution and heat flux in the problem domain. The calculated SIFs for the crack with various inclinations are presented in Figure 6 and good agreement with the results from [4] is achieved.

4.2. Curved central crack

The second example comprises an arc-shaped crack in a square domain as shown in Figure 7, the configuration of which is $w = 0.2$ m, $2a = 0.1w$, $\beta = \pi/4$. The plate is under a constant and upward heat flux $\bar{q} = 10^4$ W/m^2, where the bottom of the plate is at a high temperature and the top is at a low temperature. There is an analytical solution for this problem from Chen and Hasebe [51] when this problem is considered in an infinite

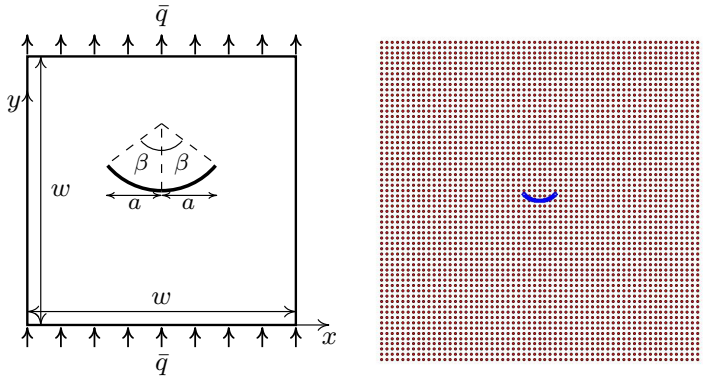

(a) (b)

Figure 7: A curved crack under constant heat flux: (a) configuration; (b) initial particle arrangement where cracking particles are in blue.

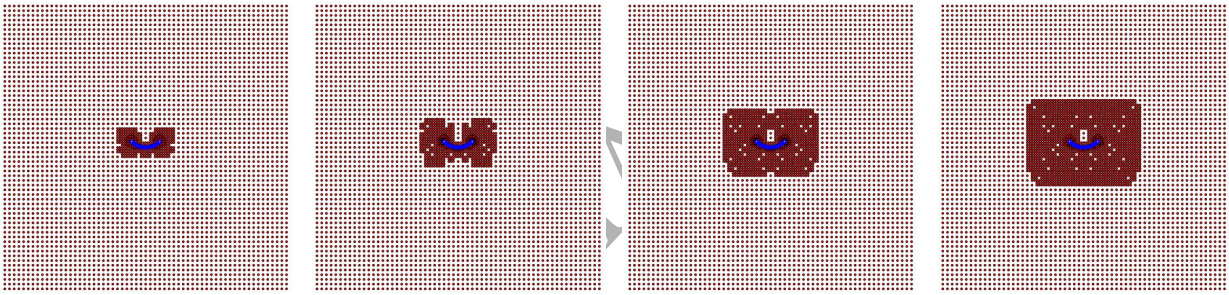

Figure 8: Adaptive particle arrangements for the curved crack problem: (a) step 2; (b) step 4; (c) step 6; (d) step 8.

plate, as

$$K_{\mathrm{I}} = \frac{3+\cos\beta}{4}\Big(\sin\frac{\beta}{2} + \frac{4(1-\cos\beta)}{(3-\cos\beta)\cos\beta}\cos\frac{\beta}{2}\Big)\frac{E\alpha\bar{q}}{k_T}a\sqrt{\pi a}, \tag{25a}$$

$$K_{\mathrm{II}} = \frac{3+\cos\beta}{4}\Big(\cos\frac{\beta}{2} - \frac{4(1-\cos\beta)}{(3-\cos\beta)\sin\beta}\sin\frac{\beta}{2}\Big)\frac{E\alpha\bar{q}}{k_T}a\sqrt{\pi a}. \tag{25b}$$

For the sake of data analysis, the SIFs are normalised as

$$K_n' = \frac{K_n}{\alpha\bar{q}E}\cdot\frac{k_T}{a\sqrt{\pi a}}, \quad n \in \{\mathrm{I},\mathrm{II}\}. \tag{26}$$

Since the ratio between the size of the crack and the plate is $2a/w = 1/10$, the boundaries of this finite domain are far from the crack and the analytical solutions are applicable to this problem. The plate is initially discretised with 61×61 particles, from which the adaptivity approach proceeds. The curvature of the crack is modelled by

Table 2: Normalised SIFs for a curved crack under thermal loading

	CPM		HXFEM [12]		Analytical [51]	
θ	K'_{I}	K'_{II}	K'_{I}	K'_{II}	K'_{I}	K'_{II}
30°	0.71745	0.79217	0.73962	0.82085	0.71904	0.80793
45°	0.97096	0.58499	0.97630	0.57770	0.97338	0.59995
60°	1.12586	0.34761	1.13546	0.33238	1.13750	0.35363

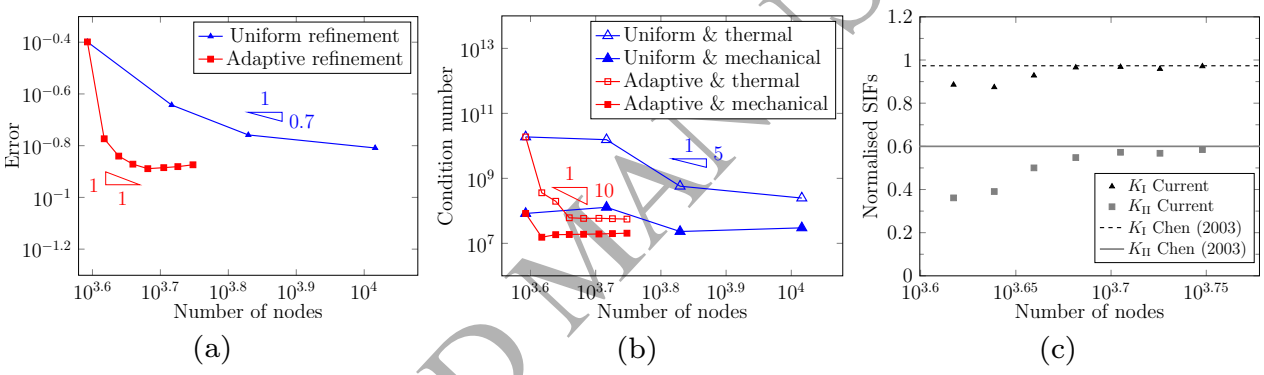

Figure 9: Adaptive results for the curved crack under thermal loading: (a) convergence rate for error; (b) condition number and (c) SIFs, where analytical results are from Chen and Hasebe [51]

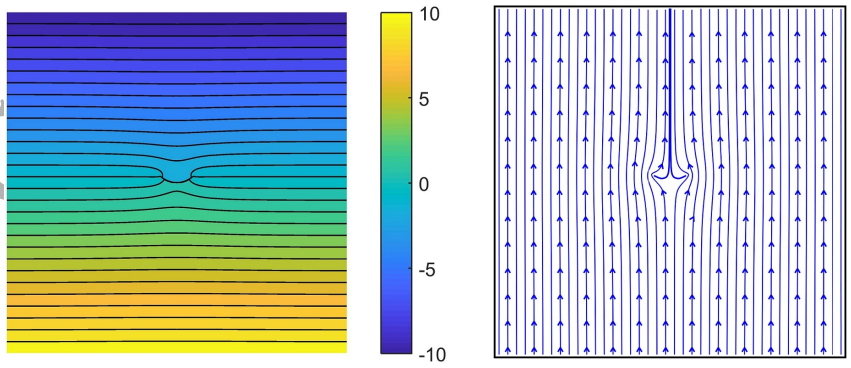

Figure 10: Thermal results for the curved crack problem: (a) temperature profile (°C); (b) heat flux.

41 cracking particles (with straight segments connecting them), which are in blue in Figure 7 (b).

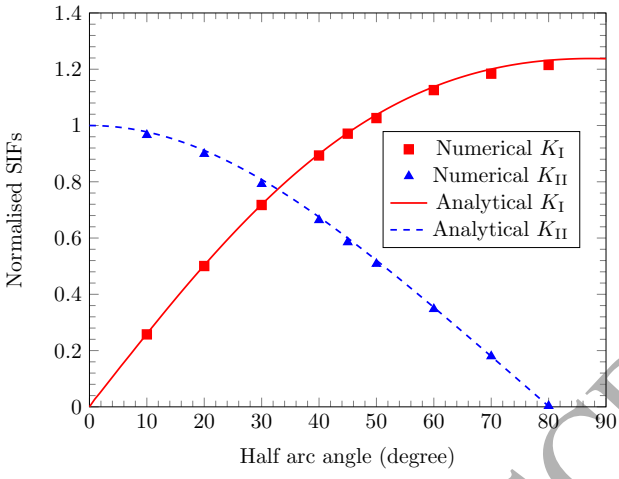

Figure 11: Normalised stress intensity factors for the curved crack with various values of the half arc angle.

The adaptivity approach uses a target error of $\eta_t = 0.12$ and adaptive particle distributions are shown in Figure 8. The local zone containing the crack is refined and two "masses" of particles are generated around the two crack tips. Particle refinement is also executed at both the top and bottom where the heat flux boundary condition is applied. Results including global error, the condition number of system stiffness matrix and SIFs are presented in Figure 9, where adaptive refinement shows lower errors and condition numbers than uniform refinement and good agreements of SIFs with analytical solutions are evident. The results of temperature profile and heat flux distribution are given in Figure 10, where it is shown that the crack disturbs the temperature profile at the centre of the plate and the heat flux travels encircling the crack surface. SIFs are calculated and compared with the results from Zamani et al. [12] using the HXFEM in Table 2. The same level of accuracy is obtained by the proposed method with 8391 particles compared with more than 10^4 nodes in the HXFEM [12]. For the curved crack with various curvatures, the proposed method delivers accurate SIFs compared to the analytical solution from Equation (25), as given in Figure 11. It has also been shown that, even with uniformly distributed particles, the proposed method is capable of capturing the stress gradients at the crack tip of a curved crack.

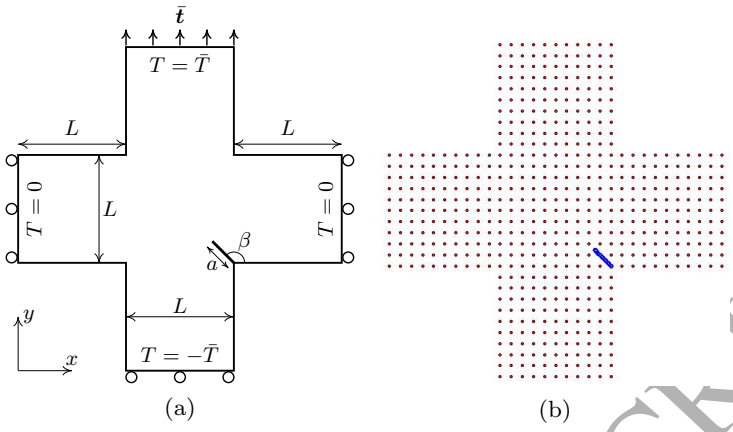

Figure 12: A crack in a cruciform shaped plate: (a) configuration; (b) initial particle arrangement (cracking particles are in blue).

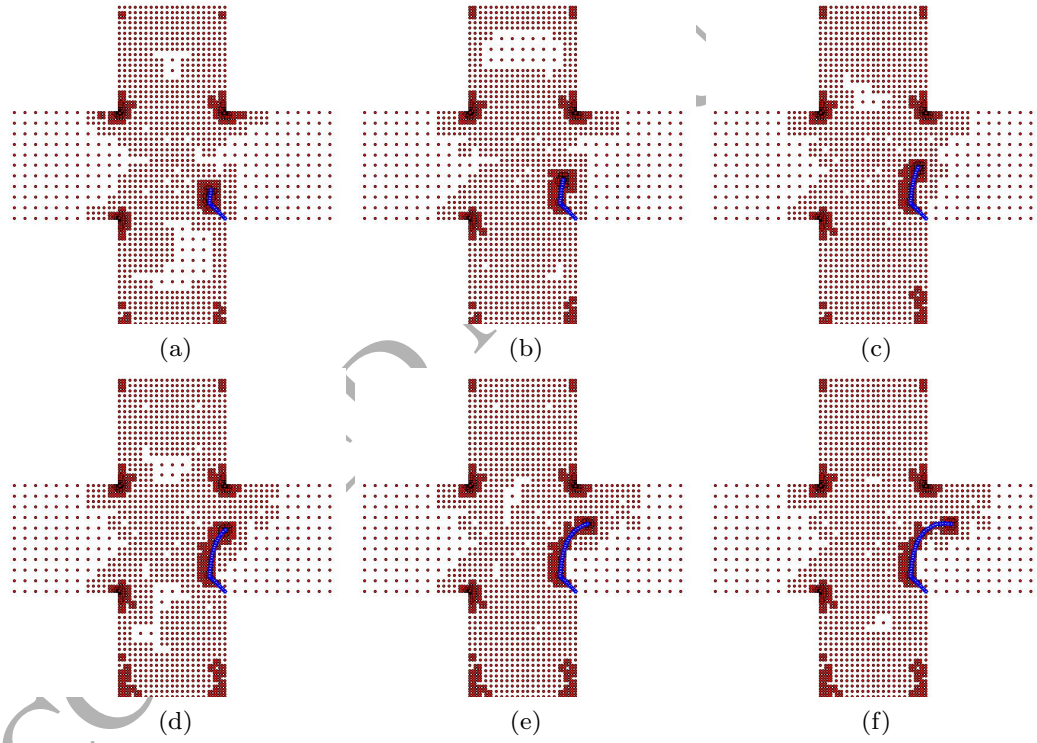

Figure 13: Adaptive particle arrangements of crack propagation steps for the cruciform shaped plate problem: (a-f) step=5, 10, 15, 20, 25 and 30.

4.3. Crack propagation in a cruciform shaped plate

Crack propagation under thermal loading is considered in the third example. The crack is located at the bottom-right corner of a cruciform shaped plate as shown in Figure 12 and the configuration is $L = 0.1$ m, $a =$

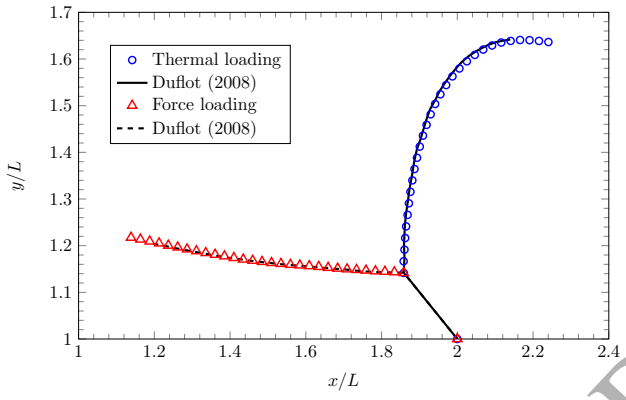

Figure 14: Comparison of crack growth in the cruciform shaped plate between under thermal loading and force loading.

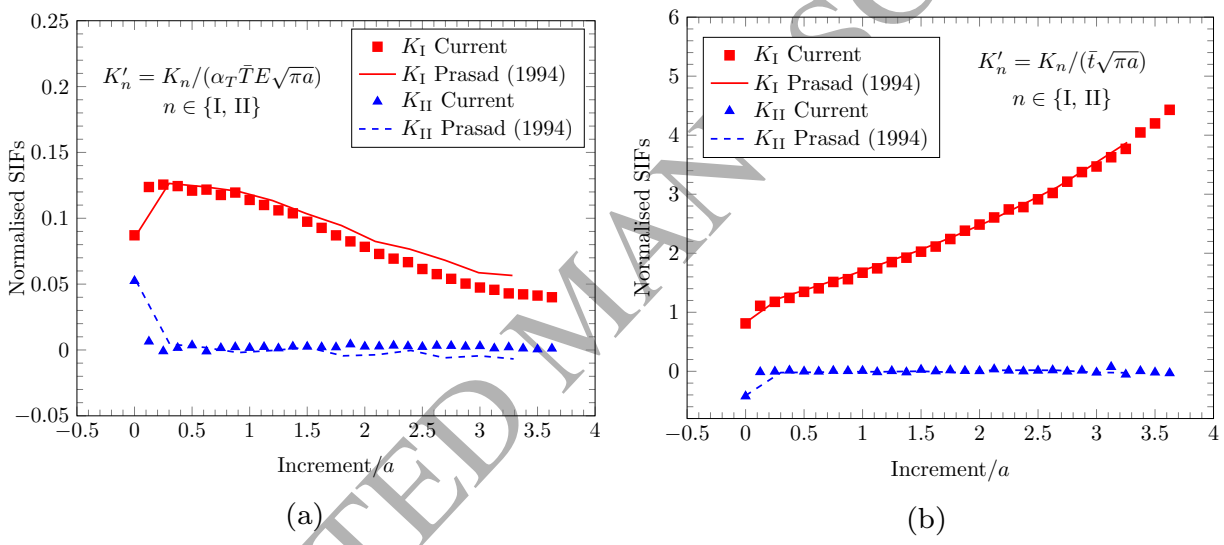

Figure 15: Normalised SIFs during crack propagation for the cruciform shaped plate problem: (a) thermal loading; (b) force loading.

$0.2L$ and $\beta = 3\pi/4$. The cruciform shaped plate is constrained in displacement at the bottom and both left and right sides. Two loading situations are considered: Case 1, thermal loading with $\bar{T} \neq 0$, $\bar{t} = 0$; Case 2, mechanical loading with $\bar{T} = 0$, $\bar{t} \neq 0$. The crack propagation direction is determined by the maximum circumferential stress criterion and the crack increment is set as $a/8$. A wide range of alternative crack propagation criteria are available, and surveys can be found in the literature, e.g. [52, 53], however the maximum circumferential stress criterion used here has been shown to be both easy to implement and robust [54].

The adaptivity approach is defined with target error $\eta_t = 0.04$ and starts from the initial particle arrangement shown in Figure 12 (b). Adaptive particle arrangements during the crack propagation for Case 1 are given in

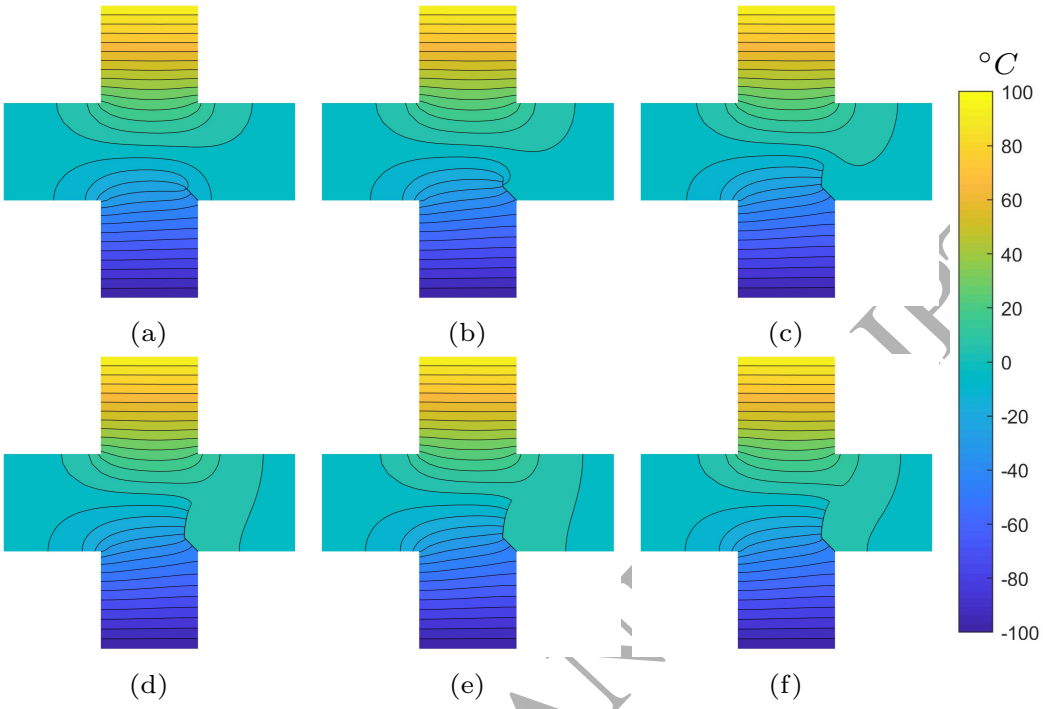

Figure 16: Temperature distribution during crack propagation steps for the cruciform shaped plate: (a-f) step=1, 5, 10, 15, 20 and 30 respectively.

Figure 13, where particle distribution is refined at the three corners of the cruciform shaped plate and the crack tip. The crack propagates upward and then turns right after 15 propagation steps. The crack growth predicted by the proposed method is compared with the results from Duflot [4] using the XFEM, where good agreement is found and similar accuracy is obtained for Case 2 as shown in Figure 14. Comparing the crack growth in the two cases, the crack propagates right under thermal loading while the mechanical loading leads the crack propagation to the left. The SIFs during crack propagation steps in the two cases are calculated, which match well with the results from Prasad et al. [55] as shown in Figure 15. The temperature profile during crack propagation steps can be seen in Figure 16, where the crack path changes the temperature distribution on the two sides of the crack. The thermal flux is also affected by the crack path as given in Figure 17, where the flux lines travel along rather than across the crack.

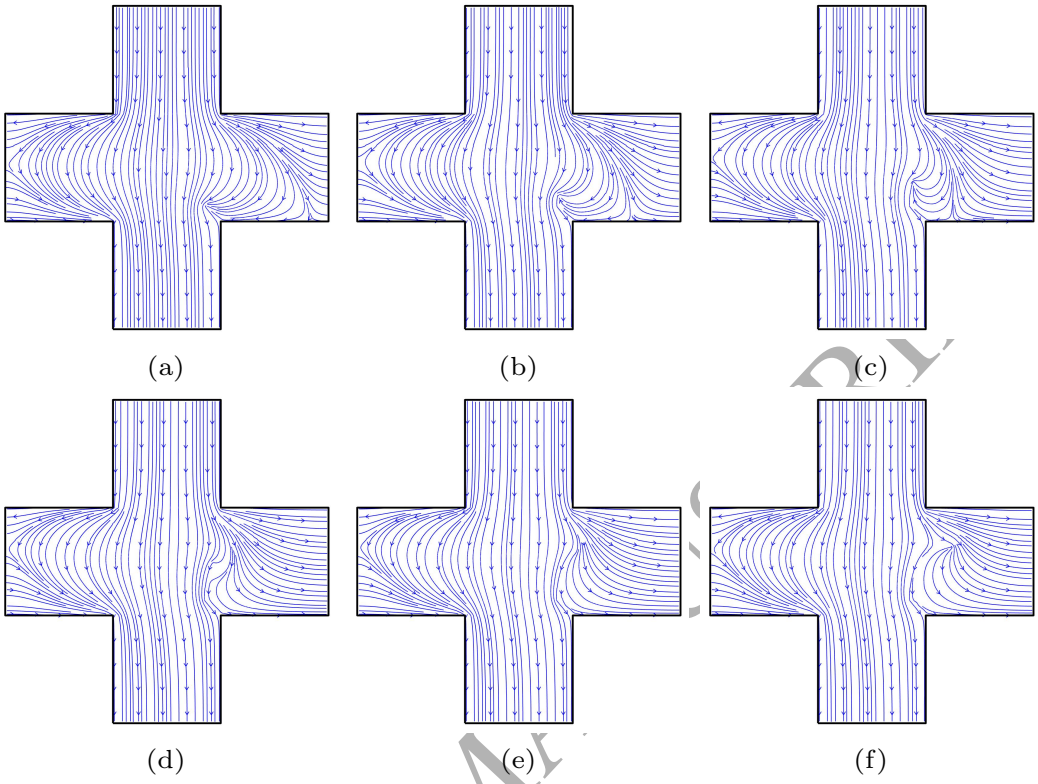

Figure 17: Thermal flux during crack propagation steps for the cruciform shaped plate: (a-f) step=1, 5, 10, 15, 20 and 30.

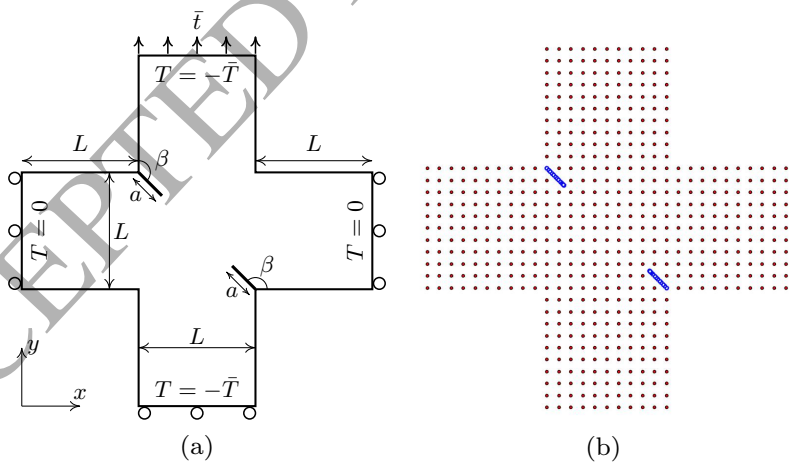

Figure 18: Two cracks in a cruciform shaped plate: (a) configuration; (b) initial particle arrangement.

4.4. Two cracks in a cruciform shaped plate

The fourth example matches the third problem with one extra crack as shown in Figure 18, and other aspects including displacement boundary conditions and material properties are identical. There are also two loading

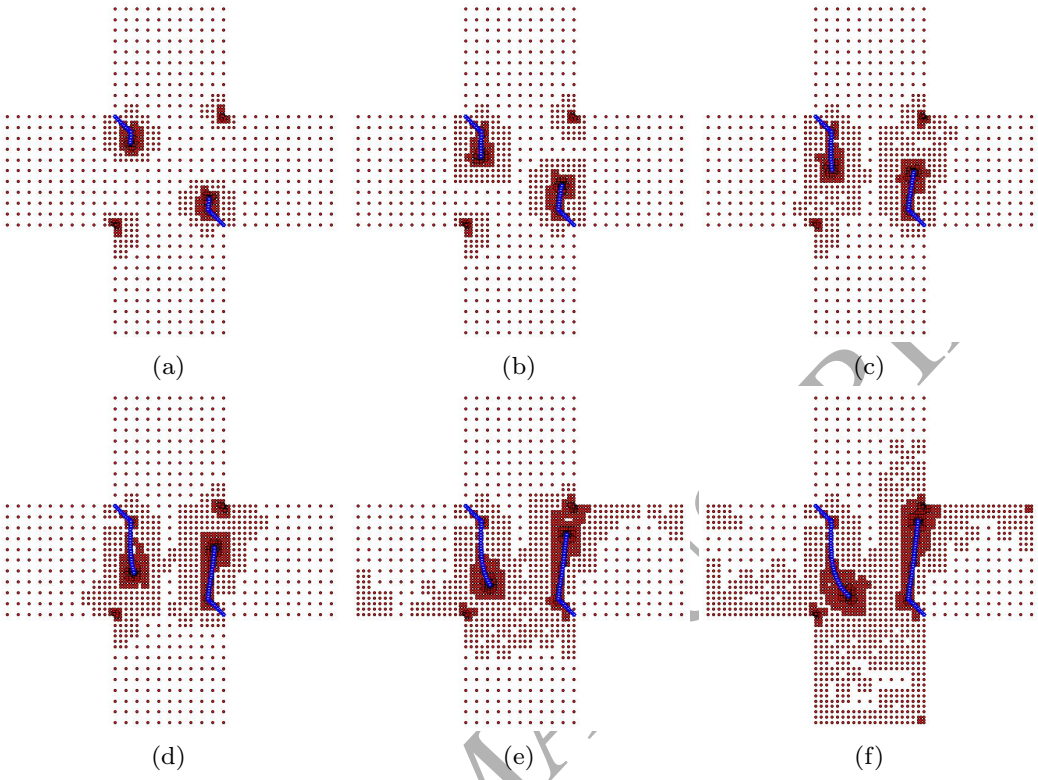

Figure 19: Adaptive particle arrangements for the two cracks in a cruciform shaped plate: (a-f) step=5, 10, 15, 20, 25 and 30.

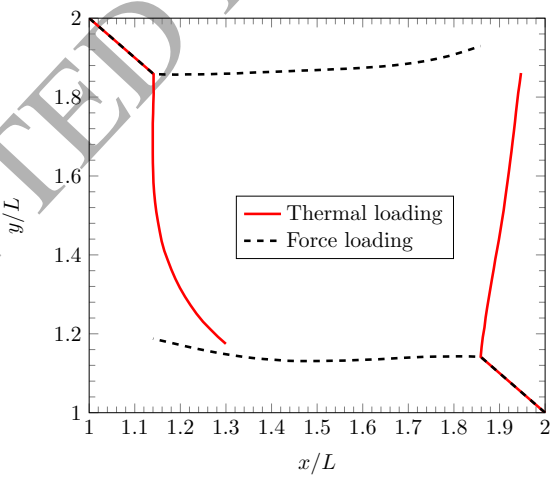

Figure 20: Propagation of two cracks in the cruciform shaped plate under thermal loading and force loading.

conditions involved, which are thermal loading and mechanical loading, and the difference is in Case 1 where the top and bottom sides of the plate are loaded by a low temperature $-\bar{T}$.

Adaptive particle distributions for the propagation of the two cracks in Case 1 are given in Figure 19, where

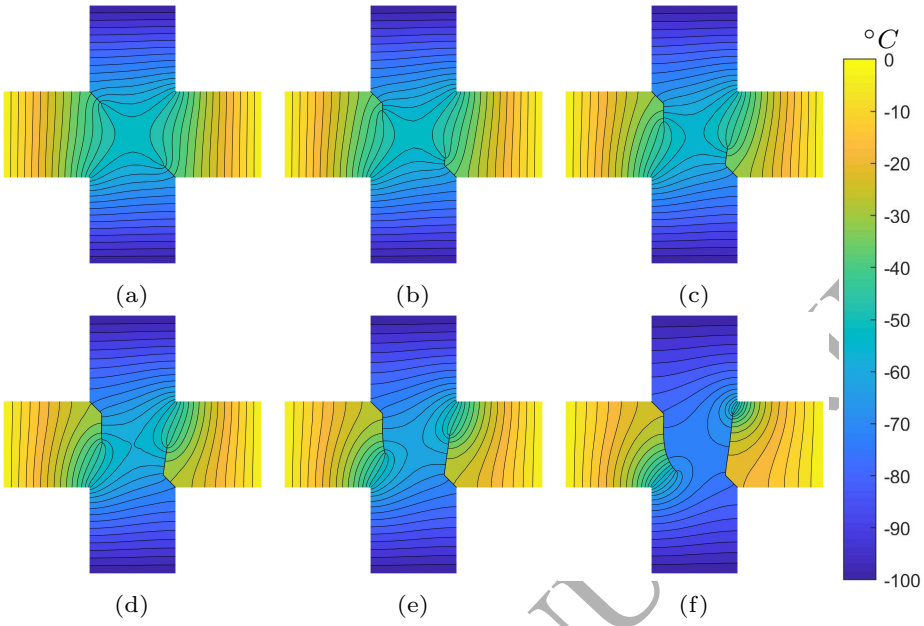

Figure 21: Temperature distribution during crack propagation steps for two cracks in the cruciform shaped plate: (a-f) step=1, 5, 10, 15, 20 and 30.

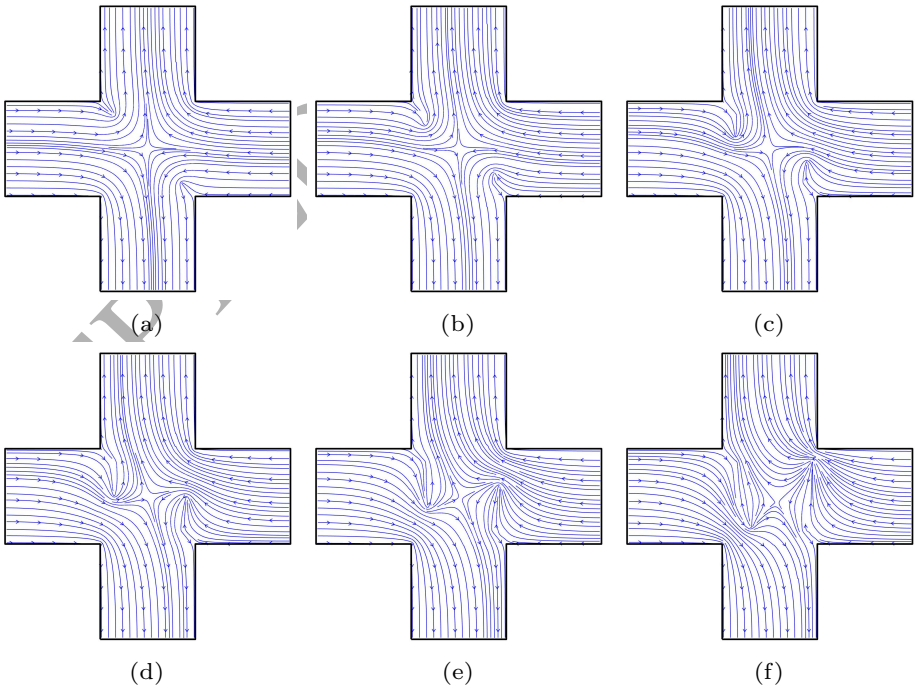

Figure 22: Thermal flux during crack propagation steps for two cracks in the cruciform shaped plate: (a-f) step=1, 5, 10, 15, 20 and 30.

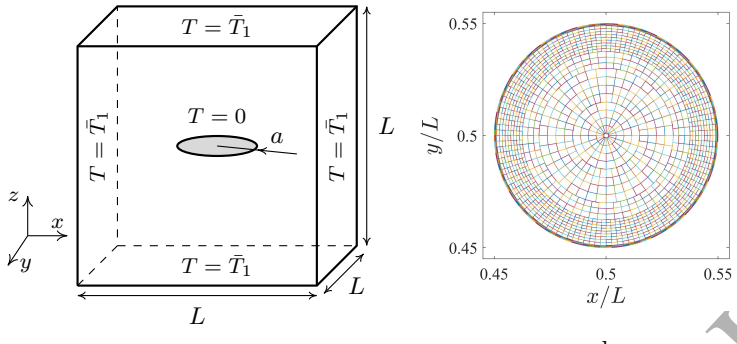

Figure 23: Configuration of a penny-shaped crack in a large medium with high temperature at all surfaces: (a) configuration and (b) integration cells to impose boundary conditions at crack surfaces.

again there are two "masses" of particles generated around the two crack tips which travel with the two crack tips during the crack propagation process. The crack on the right propagates straight upwards towards the upper-right corner, while the left crack descends and turns right after 20 propagation steps. The crack growths for both cases are given in Figure 20, where it is shown that the two cracks propagate vertically under the thermal loading here, while the mechanical loading leads to horizontal crack propagation. The temperature profile and heat flux during crack propagation steps for the two cracks are presented in Figures 21 and 22, where the considerable influence of the presence of the two cracks on both temperature distribution and heat flux direction is evident. No analytical solution has been found for this particular problem yet, and this example is used here to test the ability of the proposed methodology for modelling multiple crack propagation. The original results are included in Table 3, which can be used for comparison by researchers wishing to test their own methods.

4.5. Penny-shaped crack

A penny shaped crack problem is included to test the proposed method in 3D crack problems with the isothermal crack assumption, as presented in Figure 23. The radius of the crack is $a = 0.01$m, and the size of the cube is $L = 20a$. The surfaces of the crack are at low temperature, $T = 0$, while all surfaces of the cube are subject to a high temperature, $T = \bar{T}_1 = 100°$C. The cube is large enough so that the analytical solutions by Das [56] and Murakami et al. [57] for a penny-shaped crack in an infinite medium under thermal load is

Table 3: Crack propagation paths for the two cracks in the cruciform shaped plate under thermal loading

steps	crack 1		crack 2		steps	crack 1		crack 2	
	x/L	y/L	x/L	y/L		x/L	y/L	x/L	y/L
0	2.000	1.000	1.000	2.000	16	1.909	1.513	1.151	1.484
1	1.859	1.142	1.141	1.858	17	1.912	1.538	1.155	1.459
2	1.861	1.166	1.141	1.833	18	1.915	1.563	1.159	1.435
3	1.863	1.191	1.142	1.808	19	1.918	1.588	1.165	1.410
4	1.867	1.216	1.141	1.783	20	1.921	1.612	1.172	1.387
5	1.869	1.241	1.140	1.758	21	1.923	1.637	1.180	1.363
6	1.873	1.266	1.140	1.733	22	1.926	1.662	1.189	1.339
7	1.876	1.290	1.140	1.708	23	1.929	1.687	1.199	1.316
8	1.880	1.315	1.139	1.683	24	1.931	1.712	1.210	1.294
9	1.884	1.340	1.139	1.658	25	1.934	1.737	1.222	1.272
10	1.887	1.365	1.140	1.633	26	1.936	1.762	1.235	1.251
11	1.891	1.389	1.140	1.608	27	1.939	1.786	1.250	1.231
12	1.895	1.414	1.141	1.583	28	1.941	1.811	1.266	1.211
13	1.899	1.439	1.143	1.559	29	1.944	1.836	1.282	1.193
14	1.902	1.464	1.145	1.534	30	1.947	1.861	1.300	1.175
15	1.906	1.488	1.147	1.509					

applicable here. SIFs at the crack tip are normalised by

$$K_{\mathrm{I}}' = \frac{K_{\mathrm{I}}(1-\nu)}{\alpha_T E \bar{T}_1 \sqrt{a/\pi}}. \tag{27}$$

The error of the mode I SIF from the analytical value K_{I}^0 is measured as

$$e(K_{\mathrm{I}}) = \sum_{j=1}^{n_c} \frac{|K_{\mathrm{I}}^j - K_{\mathrm{I}}^0|}{n_c K_{\mathrm{I}}^0}, \tag{28}$$

where n_c is the number of particles at the crack front. Temperature constraints at the crack surfaces are imposed by Lagrange multipliers using Equation (14b), where shape functions N_k are calculated by the MLS

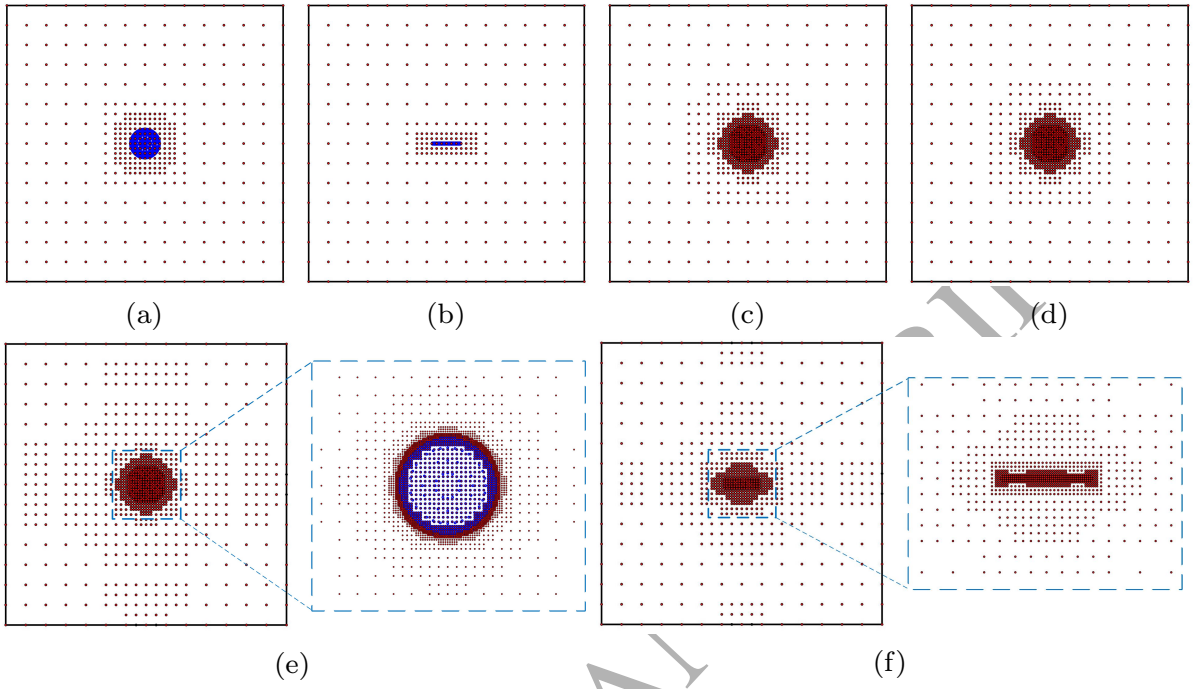

Figure 24: Adaptive refinement steps for the penny-shaped crack under thermal loading: (a) step 1 xy view; (b) step 1 xz view;(c) step 3 xy view; (d) step 3 xz view;(e) step 5 xy view; (f) step 5 xz view. Cracking particles are marked in blue.

approximation over particles on the crack surfaces and the integration cells are given in Figure 23 (b). Crack discontinuities are handled using the visibility criterion, as detailed in the 3D version of the CPM described in [38], and no other special handling is required. The cube is initially discretised with $15 \times 15 \times 15$ particles with refined particles around the crack, as shown in Figure 24 (a). Adaptive refinement steps using $\eta_t = 0.04$ are presented in Figure 24, where dense particles were generated around the crack front to capture the stress and temperature gradients. Results during adaptive steps are given in Figure 25, where adaptive refinements show better convergence than uniform refinements in global error and SIF error, while no significant differences are found for the condition numbers of the system stiffness matrix in Figure 25 (c). The SIFs agree well with the analytical solutions [57] and results from the XFEM [58] and the BEM [59] as shown in Figure 26 (a), and the temperature distribution inside the cube is presented in Figure 26 (b).

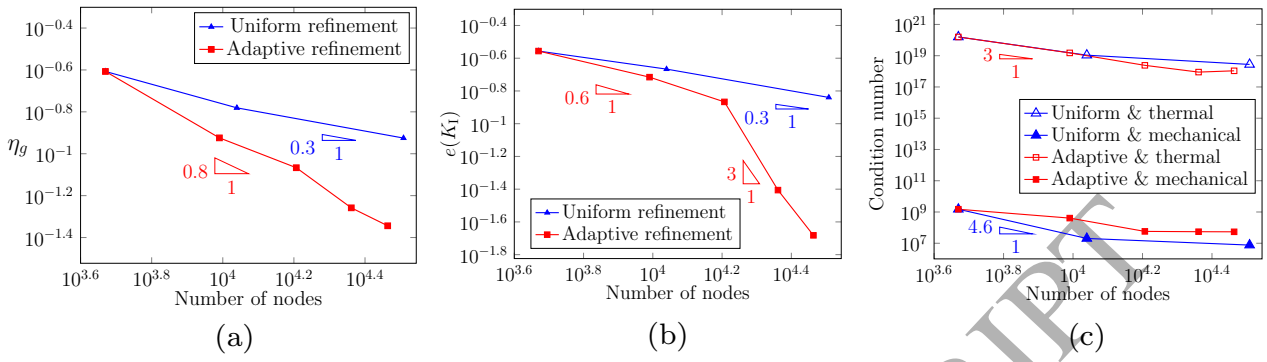

Figure 25: Adaptive results for the penny-shaped crack under thermal loading: (a) convergence rate for global error; (b) error of SIF; (c) condition number.

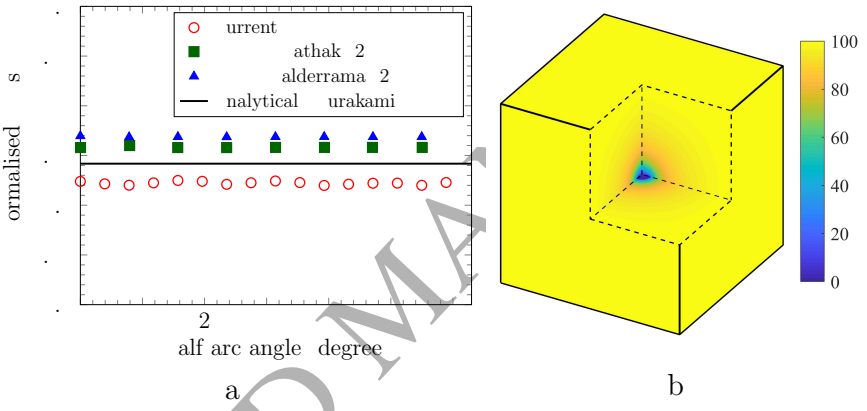

Figure 26: Results at the last adaptive step for the penny-shaped crack problem: (a) SIF and (b) temperature (°C), where a fraction of the cube (marked by dashed lines) is omitted to illustrate the temperature distribution inside.

5. Summary

An adaptive CPM for modelling thermoelastic fracture in 2D has been developed in this paper, where enrichment functions, which have been widely used in traditional numerical methods including the XFEM and the EFGM, are not required. The discontinuities of temperature and displacement at a crack are modelled by the CPM using the visibility criterion, and stress gradients are captured using a high density of particles around the crack tip, which is controlled by an adaptivity approach. The mixed-mode stress intensity factors under thermal loadings are calculated by the interaction integral and the proposed method has been shown to provide results at the same level of accuracy as the XFEM with high order enrichments while using fewer particles than the number of nodes in the standard XFEM. The proposed methodology has therefore shown its potential to

handle the crack propagation of multiple cracks under thermal loading.

Acknowledgements

W. Ai acknowledges the financial support from the China Scholarship Council (CSC) during his PhD of which this work formed a part.

References

[1] G. C. Sih, On the singular character of thermal stresses near a crack tip, J. Appl. Mech. 29 (1962) 587.

[2] M. L. Williams, C. Pasadena, On the stress distribution at the base of a stationary crack, J. Appl. Mech. 24 (1) (1957) 109–114.

[3] A. Y. Kuo, Effects of crack surface heat conductance on stress intensity factors, J. Appl. Mech. 57 (2) (1990) 354–358.

[4] M. Duflot, The extended finite element method in thermoelastic fracture mechanics, Int. J. Numer. Methods Eng. 74 (5) (2008) 827–847.

[5] X. C. Zhong, K. Y. Lee, A thermal-medium crack model, Mech. Mater. 51 (2012) 110–117.

[6] X. F. Li, K. Y. Lee, Effect of heat conduction of penny-shaped crack interior on thermal stress intensity factors, Int. J. Heat Mass Transfer 91 (2015) 127–134.

[7] E. Emmel, H. Stamm, Calculation of stress intensity factors of thermally loaded cracks using the finite element method, Int. J. Press. Vessels Pip. 19 (1) (1985) 1–17.

[8] J. Magalhaes, A. Emery, Transient thermoelastic fracture of brittle substrates bonded to brittle films, J. Therm. Stresses 20 (1) (1997) 35–45.

[9] H. Chen, Q. Wang, G. Liu, Y. Wang, J. Sun, Simulation of thermoelastic crack problems using singular edge-based smoothed finite element method, Int. J. Mech. Sci. 115 (2016) 123–134.

[10] N. Prasad, M. Aliabadi, D. Rooke, The dual boundary element method for thermoelastic crack problems, Int. J. Fract. 66 (3) (1994) 255–272.

[11] L. Wrobel, C. Brebbia, The dual reciprocity boundary element formulation for nonlinear diffusion problems, Comput. Methods Appl. Mech. Eng. 65 (2) (1987) 147–164.

[12] A. Zamani, R. Gracie, M. R. Eslami, Higher order tip enrichment of extended finite element method in thermoelasticity, Comput. Mech. 46 (6) (2010) 851–866.

[13] A. Zamani, M. R. Eslami, Implementation of the extended finite element method for dynamic thermoelastic fracture initiation, Int. J. Solids Struct. 47 (10) (2010) 1392–1404.

[14] M. Pant, I. Singh, B. Mishra, Numerical simulation of thermo-elastic fracture problems using element free Galerkin method, Int. J. Mech. Sci. 52 (12) (2010) 1745–1755.

[15] S. Wang, H. Zhang, Partition of unity-based thermomechanical meshfree method for two-dimensional crack problems, Arch. Appl. Mech. 81 (10) (2011) 1351–1363.

[16] L. Bouhala, A. Makradi, S. Belouettar, Thermal and thermo-mechanical influence on crack propagation using an extended mesh free method, Eng. Fract. Mech. 88 (2012) 35–48.

[17] H. Wang, An extended element-free Galerkin method for thermo-mechanical dynamic fracture in linear and nonlinear materials, Comput. Mater. Sci. 98 (2015) 366–371.

[18] H. Zhang, G. Ma, F. Ren, Implementation of the numerical manifold method for thermo-mechanical fracture of planar solids, Eng. Anal. Boundary Elem. 44 (2014) 45–54.

[19] H. Zhang, G. Ma, L. Fan, Thermal shock analysis of 2D cracked solids using the numerical manifold method and precise time integration, Eng. Anal. Boundary Elem. 75 (2017) 46–56.

[20] H. Bayesteh, A. Afshar, S. Mohammdi, Thermo-mechanical fracture study of inhomogeneous cracked solids by the extended isogeometric analysis method, Eur. J. Mech. A-Solids 51 (2015) 123–139. doi:10.1016/j.euromechsol.2014.12.004.

[21] D. Simkins, S. Li, Meshfree simulations of thermo-mechanical ductile fracture, Comput. Mech. 38 (3) (2006) 235–249.

[22] S. Wu, S. Zhang, Z. Xu, Thermal crack growth-based fatigue life prediction due to braking for a high-speed railway brake disc, Int. J. Fatigue 87 (2016) 359–369.

[23] C. Song, Analysis of singular stress fields at multi-material corners under thermal loading, Int. J. Numer. Methods Eng. 65 (5) (2006) 620–652.

[24] C. Li, E. T. Ooi, C. Song, S. Natarajan, SBFEM for fracture analysis of piezoelectric composites under thermal load, Int. J. Solids Struct. 52 (2015) 114–129.

[25] E. T. Ooi, C. Song, F. Tin-Loi, Z. Yang, Polygon scaled boundary finite elements for crack propagation modelling, Int. J. Numer. Methods Eng. 91 (3) (2012) 319–342.

[26] S. Dai, C. Augarde, C. Du, D. Chen, A fully automatic polygon scaled boundary finite element method for modelling crack propagation, Eng. Fract. Mech. 133 (2015) 163–178.

[27] A. Menk, S. P. Bordas, A robust preconditioning technique for the extended finite element method, Int. J. Numer. Methods Eng. 85 (13) (2011) 1609–1632.

[28] K. Agathos, E. Chatzi, S. P. Bordas, A unified enrichment approach addressing blending and conditioning issues in enriched finite elements, Comput. Meth. Appl. Mech. Eng. 349 (2019) 673–700.

[29] K. Agathos, S. P. Bordas, E. Chatzi, Improving the conditioning of XFEM/GFEM for fracture mechanics problems through enrichment quasi-orthogonalization, Comput. Meth. Appl. Mech. Eng. 346 (2019) 1051–1073.

[30] H. P. Bui, S. Tomar, S. P. Bordas, Corotational cut finite element method for real-time surgical simulation: Application to needle insertion simulation, Comput. Meth. Appl. Mech. Eng. 345 (2019) 183–211.

[31] E. Barbieri, N. Petrinic, M. Meo, V. Tagarielli, A new weight-function enrichment in meshless methods for multiple cracks in linear elasticity, Int. J. Numer. Methods Eng. 90 (2) (2012) 177–195.

[32] E. Barbieri, N. Petrinic, Three-dimensional crack propagation with distance-based discontinuous kernels in meshfree methods, Comput. Mech. 53 (2) (2014) 325–342.

[33] W. Ai, C. E. Augarde, An adaptive cracking particle method for 2D crack propagation, Int. J. Numer. Methods Eng. 108 (13) (2016) 1626–1648.

[34] Z. Yosibash, Numerical thermo-elastic analysis of singularities in two-dimensions, Int. J. Fract. 74 (4) (1996) 341–361.

[35] T. Rabczuk, T. Belytschko, Cracking particles: a simplified meshfree method for arbitrary evolving cracks, Int. J. Numer. Methods Eng. 61 (13) (2004) 2316–2343.

[36] T. Rabczuk, T. Belytschko, A three-dimensional large deformation meshfree method for arbitrary evolving cracks, Comput. Methods Appl. Mech. Eng. 196 (29) (2007) 2777–2799.

[37] T. Rabczuk, G. Zi, S. Bordas, H. Nguyen-Xuan, A simple and robust three-dimensional cracking-particle method without enrichment, Comput. Methods Appl. Mech. Eng. 199 (37) (2010) 2437–2455.

[38] W. Ai, C. E. Augarde, An adaptive cracking particle method providing explicit and accurate description of 3D crack surfaces, Int. J. Numer. Methods Eng. 114 (2018) 1291–1309.

[39] V. Kumar, A. Ghosh, Non-linear dynamic fragmentation using cracking particles method, Comput. Mater. Sci. 98 (2015) 117–122.

[40] V. Kumar, R. Drathi, A meshless cracking particles approach for ductile fracture, KSCE J. Civ. Eng. 18 (1) (2014) 238–248.

[41] T. Rabczuk, P. Areias, T. Belytschko, A simplified mesh-free method for shear bands with cohesive surfaces, Int. J. Numer. Methods Eng. 69 (5) (2007) 993–1021.

[42] T. Rabczuk, E. Samaniego, Discontinuous modelling of shear bands using adaptive meshfree methods, Comput. Methods Appl. Mech. Eng. 197 (6) (2008) 641–658.

[43] W. Ai, C. E. Augarde, A multi-cracked particle method for complex fracture problems in 2D, Math. Comput. Simul 150 (2018) 1–24.

[44] T. Belytschko, Y. Lu, L. Gu, Element-free Galerkin methods, Int. J. Numer. Methods Eng. 37 (2) (1994) 229–256.

[45] E. Rabizadeh, A. S. Bagherzadeh, T. Rabczuk, Goal-oriented error estimation and adaptive mesh refinement in dynamic coupled thermoelasticity, Comput. Struct. 173 (2016) 187–211.

[46] C. K. Lee, C. Zhou, On error estimation and adaptive refinement for element free Galerkin method: Part I: stress recovery and a posteriori error estimation, Comput. Struct. 82 (4) (2004) 413–428.

[47] H. Chung, T. Belytschko, An error estimate in the EFG method, Comput. Mech. 21 (2) (1998) 91–100.

[48] J. Yau, S. Wang, H. Corten, A mixed-mode crack analysis of isotropic solids using conservation laws of elasticity, J. Appl. Mech. 47 (2) (1980) 335–341.

[49] X. Zhuang, C. Heaney, C. Augarde, On error control in the element-free Galerkin method, Eng. Anal. Boundary Elem. 36 (3) (2012) 351 – 360.

[50] R. Bird, W. Coombs, S. Giani, A quasi-static discontinuous Galerkin configurational force crack propagation method for brittle materials, Int. J. Numer. Methods Eng. 113 (7) (2018) 1061–1080.

[51] Y. Chen, N. Hasebe, Solution for a curvilinear crack in a thermoelastic medium, J. Therm. Stresses 26 (3) (2003) 245–259.

[52] P. O. Bouchard, F. Bay, Y. Chastel, Numerical modelling of crack propagation: automatic remeshing and comparison of different criteria, Comput. Methods Appl. Mech. Eng. 192 (35) (2003) 3887–3908.

[53] W. Ai, R. E. Bird, W. M. Coombs, C. E. Augarde, A configurational force driven cracking particle method for modelling crack propagation in 2D, Eng. Anal. Boundary Elem. 104 (2019) 197–208.

[54] W. Ai, Computational fracture modelling by an adaptive cracking particle method, Ph.D. thesis, Durham University (2018).

[55] N. Prasad, M. Aliabadi, D. Rooke, Incremental crack growth in thermoelastic problems, Int. J. Fract. 66 (3) (1994) R45–R50.

[56] B. R. Das, Thermal stresses in a long cylinder containing a penny-shaped crack, Int. J. Eng. Sci. 6 (9) (1968) 497–516.

[57] Y. Murakami, L. Keer, Stress intensity factors handbook, vol. 3, J. Appl. Mech. 60 (1993) 1063.

[58] H. Pathak, A. Singh, I. Singh, S. Yadav, Fatigue crack growth simulations of 3-D linear elastic cracks under thermal load by XFEM, Front. Struct. Civ. Eng. 9 (4) (2015) 359–382.

[59] R. Balderrama, A. Cisilino, M. Martinez, Boundary element method analysis of three-dimensional thermoelastic fracture problems using the energy domain integral, J. Appl. Mech. 73 (6) (2006) 959–969.